Research Article | Vol. 33, No. 13 / 30 Jun 2025 / Optics Express 27929
Optics EXPRESS

Advanced characterization and parameter extraction of electrically injected InGaAs/GaAs nano-ridge lasers monolithically integrated on silicon

ANDUALEM ALI YIMAM,[1,*] DAVIDE COLUCCI,[1,2] CHARLES CAER,[2,3] DIDIT YUDISTIRA,[2] YANNICK DE KONINCK,[2,4] HUSEYIN SAR,[2] MARINA BARYSHNIKOVA,[2] PETER VERHEYEN,[2] JORIS VAN CAMPENHOUT,[2] BERNARDETTE KUNERT,[2] DRIES VAN THOURHOUT,[1] AND GEERT MORTHIER[1]

[1]*Department of Information Technology (INTEC), Photonics Research Group, Ghent University-imec, Technologiepark-Zwijnaarde 126, 9052 Ghent, Belgium*
[2]*imec, Kapeldreef 75, 3001 Heverlee, Leuven, Belgium*
[3]*Present address: Centre Suisse d'Electronique et de Microtechnique SA (CSEM), CH-2002 Neuchâtel, Switzerland*
[4]*Present address: NVidia Corporation, Roskilde 4000, Denmark*
[*]*ayimam.yimam@ugent.be*

Abstract: The static and dynamic characteristics of electrically injected monolithic nano-ridge lasers emitting around the wavelength of 1030 nm are comprehensively investigated, providing critical insights into their performance and identifying pathways for future improvement. Key laser parameters such as the D-factor, the K-factor, the differential gain and the gain compression factor are extracted. Recombination coefficients and carrier escape times are determined by taking the effective carrier capture times derived from the small-signal modulation response. Additionally, the impact of the nano-ridge box size on the recombination coefficients is evaluated, highlighting the role of structural design in optimizing device performance and reliability.

1. Introduction

Silicon photonics has emerged as a transformative technology platform for addressing the increasing demands of high-bandwidth, power-efficient, and cost-effective optical interconnects in data centers, telecommunications and high-performance computing. It leverages the well-established complementary metal-oxide-semiconductor (CMOS) fabrication processes, ensuring scalability and lower production costs [1]. However, silicon's indirect bandgap limits its ability to efficiently emit light, necessitating the incorporation of III-V materials, which exhibit superior optical gain and carrier recombination properties. Various techniques have been explored over the years to integrate III-V materials with silicon, including flip-chip bonding [2], die-to-wafer bonding [3–5], and transfer printing [6,7].

On the other hand, scalability and cost-effectiveness make the monolithic integration of III-V materials on silicon a highly attractive solution for large-scale production. However, this approach presents significant challenges due to the large mismatch in crystal lattice constants, thermal expansion coefficients and polarity, all of which contribute to defect formation and hinder efficient laser performance [8]. To overcome these issues, various techniques have been explored, including the use of thick buffer layers [9,10] and aspect ratio trapping [11,12]. More recently, nano-ridge engineering has emerged as a promising strategy, leveraging selective area growth into

#566045 https://doi.org/10.1364/OE.566045
Journal © 2025 Received 24 Apr 2025; revised 6 Jun 2025; accepted 9 Jun 2025; published 23 Jun 2025

Optics EXPRESS

trenches and aspect ratio trapping to confine defects, followed by the outgrowth of high-quality III-V nano-ridges beyond the trenches [13]. This method has enabled the demonstration of optically pumped lasers emitting at wavelengths around 1020 nm [14] and 1300 nm [15].

Despite these advances, electrically injecting such small devices while maintaining low metal contact losses remained a major challenge for some time. However, this hurdle was recently overcome through the exploitation of a mode-beating effect [16], leading to the demonstration of continuous-wave lasing around 1030 nm at room-temperature for electrically pumped $In_{0.2}Ga_{0.8}As$/GaAs quantum well nano-ridge lasers. Notably, these devices were fabricated on standard 300 mm Si (001) wafers entirely within a CMOS pilot manufacturing line, highlighting their compatibility with existing semiconductor fabrication processes. Furthermore, we recently introduced a semi-analytical model that provides deeper insights into the operating principles of these lasers [17]. This model enables a comprehensive analysis of how various device parameters influence the spectral behavior, the slope efficiency and the threshold gain, offering a valuable tool for optimizing future designs.

In this work, we conduct a comprehensive investigation of the static and dynamic characteristics of these lasers, offering key insights into their performance and potential areas for improvement. To enhance clarity and understanding, we present a full characterization of a single device throughout the paper while also including data from additional devices to illustrate the dependence on structural parameters.

Section 2 covers the static characterization of the device, while Sections 3 and 4 focus on extracting fundamental laser parameters such as the D-factor, the K-factor, the effective carrier capture time, the differential gain, and the gain compression factor using small-signal modulation response and relative intensity noise (RIN) measurements. Finally, in Section 5, we determine the recombination coefficients and carrier escape times based on the effective carrier capture times obtained from the small-signal modulation response measurements. Additionally, we analyze how the nano-ridge box size influences defect-related, radiative, and Auger recombination coefficients, emphasizing the critical role of structural design in optimizing device performance.

2. Static performance characterization

2.1. Structure

Figure 1 illustrates the structure of the nano-ridge laser. The active region consists of three $In_{0.2}Ga_{0.8}As$ quantum wells (QWs), embedded within a GaAs barrier. The n-type contact is formed by a tungsten plug that connects to a heavily doped n-type Si substrate, which in turn is electrically linked to the n-type GaAs region extending from the V-groove through the trench to the nano-ridge box. The p-type contact is achieved via a periodic pattern of tungsten plugs that penetrates the top InGaP layer, making contact with the p-type GaAs. The period is carefully chosen to induce mode beating between the fundamental and a higher-order mode along the device length, creating low intensity zones beneath the metal plugs. Nano-ridges with wider trench widths (denoted by 'c' in Fig. 1) exhibit larger box heights ('a') and widths ('b'). Detailed descriptions of the device design and operational mechanisms of the nano-ridge lasers can be found in [16] and [17]. For the characterized devices in this work, the laser cavity is formed by one cleaved facet and another facet formed by dry etching, which has an angle of 12° with the vertical axis [16].

2.2. Characterization

For the light-current-voltage (LIV) characterization, the lasers are operated under direct current (DC) conditions at room temperature. The emitted laser light is collected from a cleaved facet using a lensed single-mode fiber (SMF), which is connected to a power meter. Figure 2(a) illustrates the voltage and light output as function of the drive current for a device with a cavity

Optics EXPRESS

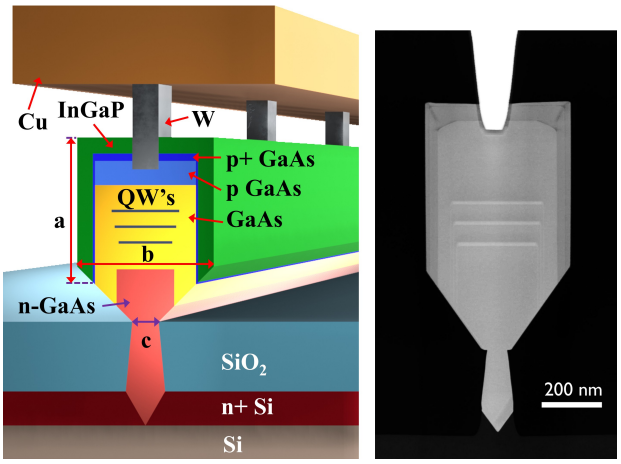

Fig. 1. Schematic of a nano-ridge laser stack and a high-angle annular dark-field scanning transmission electron microscopy (HAADF-STEM) image of an 80 nm trench nano-ridge cross-section. In the schematic, the deposited oxide which is present in the layer stack is omitted for easier visualization.

length of 1.25 mm. From the IV curve, the turn-on voltage is found to be around 1.4 V, while the light-current (LI) plot indicates a threshold current of 7 mA.

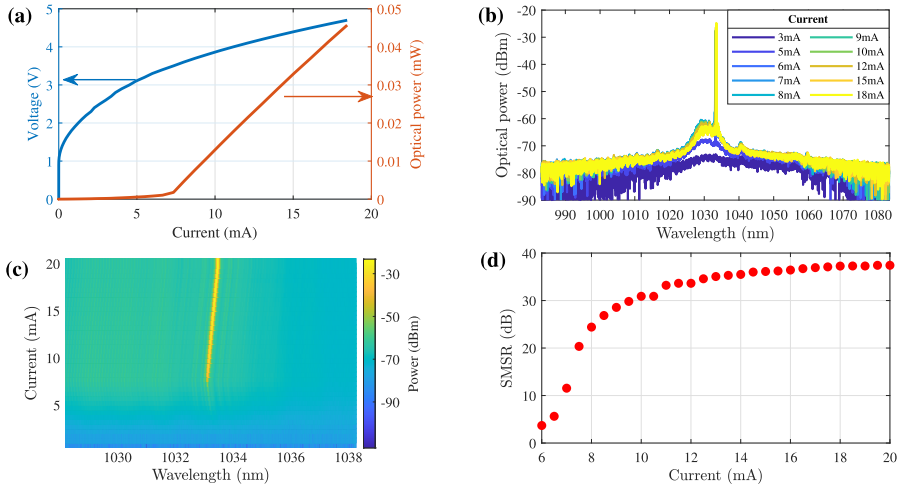

Fig. 2. (a) Current versus voltage and optical output power characteristics. (b) and (c) are 100 nm span spectra and and a 10 nm span 2D spectra at different current levels respectively. (d) SMSR of the lasing mode versus the drive current.

Using the same setup, the lensed fiber is connected to an optical spectrum analyzer (OSA) with a resolution of 0.03 nm to measure the laser spectra over a 100 nm span at various bias currents, as shown in Fig. 2(b). A 2D plot of the spectra around the lasing wavelength is depicted in Fig. 2(c). The 2D plot demonstrates single-mode operation with no mode hopping. The corresponding side-mode suppression ratio (SMSR), shown in Fig. 2(d), approaches 40 dB at a drive current approximately three times the threshold current.

Optics EXPRESS

3. Small signal modulation response measurements

For the measurement of the small signal modulation response, a DC bias current together with a small-signal modulation is injected into the laser diodes via a high-speed microwave picoprobe. Laser emission is again collected from the cleaved facet via a single mode lensed fiber, which is connected to a 1.6 GHz balanced photodetector. The electrical output from the photodetector is then sent to a network analyzer.

The modulation response of the laser, considering the effects of carrier transport is expressed as [18]:

$$H(\omega) = \frac{{\omega_r}^2}{({\omega_r}^2 - \omega^2 + j\omega\gamma)(1 + j\omega\tau_s)} \tag{1}$$

where τ_s is the effective carrier capture time, ω_r is the angular resonance frequency and γ is the damping factor.

Figure 3(a) shows the measured modulation response of the device discussed in the previous section for current injection levels above the threshold, ranging from 8 mA to 9.2 mA in increments of 0.2 mA. The figure also includes curve fits based on Eq. (1), from which the key laser parameters of $f_r = \omega_r/2\pi$, τ_s and γ were extracted.

Table 1. List of characterized nano-ridge lasers along with their key characteristics

Device No.	*Die No.*	*Length* (μm)	I_{th} (mA)	*Trench width* (nm)	*Contact pitch* (μm)	α_d (cm^{-1})	α_s (cm^{-1})	α_m (cm^{-1})
1	1	1239	7.6	100	4.6	6.1	8.5	17.2
2	1	1288	7.0	100	4.8	6.1	8.5	16.5
3	2	1248	7.0	100	4.9	6.1	8.5	17.0
4	1	1299	10.0	100	5.4	6.1	8.5	16.4
5	3	1804	9.9	80	5.4	6.8	8.5	11.6
6	3	1798	11.0	80	5.4	6.8	8.5	11.6
7	3	1796	12.0	100	4.6	6.1	8.5	11.8
8	3	1798	11.4	100	5.4	6.1	8.5	11.8
9	3	1799	9.5	100	4.9	6.1	8.5	11.8

Employing a rate equation analysis, the increase in the resonance frequency and the damping rate with current above the threshold can be quantified using the D-factor and the K-factor [19]:

$$f_r = D\sqrt{I - I_{th}} \quad \text{where} \quad D = \frac{1}{2\pi}\sqrt{\frac{\eta_i \Gamma v_g g'/\chi}{qV}} \tag{2}$$

$$\gamma = K{f_r}^2 + \gamma_0 \quad \text{where} \quad K = 4\pi^2\left(\tau_p + \frac{\varepsilon}{v_g(g'/\chi)}\right) \tag{3}$$

where η_i is the injection efficiency, Γ is the optical confinement factor, v_g is the group velocity, V is the active region volume, q is the elementary charge, g' is the differential gain, τ_p is the photon lifetime and ε is the gain compression factor considering average photon density in the cavity. $\chi = 1 + \tau_s/\tau_e$ is the transport factor where τ_e denotes the carrier escape time from the quantum wells. A more detailed discussion on the carrier escape time will be presented in Section 5.

Figure 3(b) shows the extracted resonance frequencies plotted against the square root of the bias current minus the threshold current. A linear fit to this data, based on Eq. (2), yields a D-factor of 1.072 GHz/mA$^{1/2}$. Figure 3(c) presents the damping factor as a function of the square of the resonance frequency. From a linear fit using Eq. (3), the K-factor is determined to

Optics EXPRESS

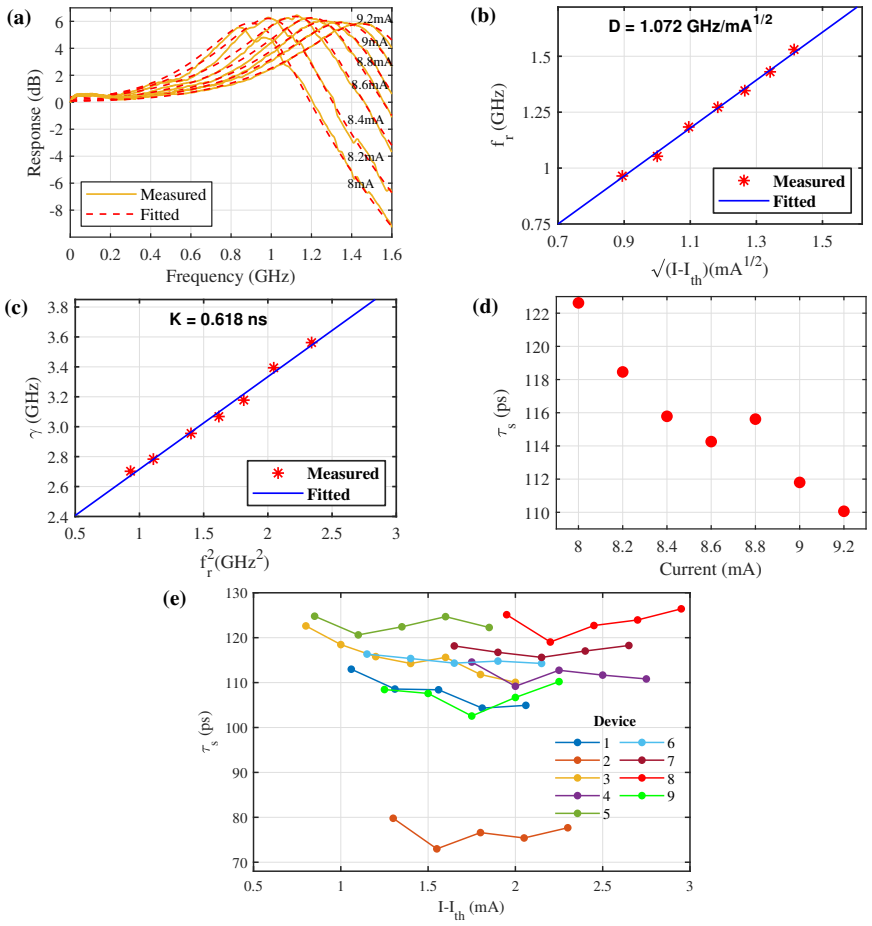

Fig. 3. (a) Small-signal modulation responses of device 3 in Table 1 at bias currents above threshold, with corresponding curve fits. (b) Extracted resonance frequencies as a function of the square root of the bias current minus the threshold current. (c) Extracted damping factors versus f_r^2. (d) Extracted effective carrier capture times at bias points above the threshold current. (e) Effective carrier capture times at bias points above threshold for the devices listed in Table 1.

be 0.618 ns, corresponding to a damping-limited maximum bandwidth of 14 GHz. Furthermore, the extracted effective carrier capture times are around 115 ps as shown in Fig. 3(d).

Using the same procedure, D-factors, K-factors and effective carrier capture times were extracted from S21 measurements performed on eight additional devices. The key laser and structural parameters of these devices are summarized in Table 1. The characterization results depicted in Figs. 3(a) through 3(d) correspond specifically to device 3 from the list. The summary of the extracted D and K-factors will be discussed in the next section, while the effective carrier capture times are presented in Fig. 3(e). With the exception of one outlier, the lasers exhibit effective carrier capture times predominantly within the range of 100-125 ps. These effective capture times reflect a combination of carrier transport and carrier capture effects [20]. Notably, the extracted effective carrier capture times are slightly higher than the typical range of 20–100 ps reported for quantum well lasers [18]. This deviation is likely due to the sparse placement of the metal plugs in the device's contacting scheme, which results in significant carrier transport

Optics EXPRESS

times. These prolonged transport times contribute to the overall effective carrier capture time in the quantum wells, ultimately affecting the dynamic properties of the lasers.

4. Relative intensity noise measurements

For the relative intensity noise (RIN) measurement of the nano-ridge lasers, we employed the subtraction method due to the lack of instrumentation capable of directly measuring RIN around the emission wavelength of 1030 nm. In the experiment, the laser emission is again collected using a single-mode lensed fiber, which is connected to a 1.6 GHz photodetector with a transimpedance gain of 16×10^3 V/A. The DC photocurrent is monitored via the integrated monitor outputs of the photodetector. The receiver's output is then passed through a DC blocker (SHF DCB-65B) to block any DC components, with the AC output routed to a 44 GHz electrical spectrum analyzer (ESA) for analysis.

To implement the subtraction method, we conduct two experiments with the laser source on and off. When the laser is on, the measured signal N_{ON} includes noise contributions from the laser itself, as well as shot noise from the photodetector N_{shot} and thermal noise N_{OFF} from the optical receiver and the ESA. When the laser is off, the detected signal corresponds solely to the thermal noise of the system, which is independent of the laser power level. The laser RIN is now given by [21]:

$$RIN(f) = \frac{\frac{N_{ON}(f) - N_{OFF}(f)}{G(f)\Delta f} - N_{shot}}{P_{elec}} \tag{4}$$

where $G(f)$ is the amplification power gain, Δf is the resolution bandwidth of the ESA, $N_{shot} = 2qI_{dc}R_L$ is the photodetector shot noise power density, I_{dc} being the photocurrent and R_L the load resistance (50 Ω). $P_{elec} = I_{dc}^2 R_L$ is the average electrical power of the photodetector.

Once the RIN is obtained via the subtraction method, the resulting spectra are fitted to curves based on a model derived from the rate equations incorporating Langevin noise sources [18,19].

$$\frac{RIN(f)}{\Delta f} = 16\pi(\Delta\nu)_{ST} \frac{\frac{1}{(2\pi\chi\tau_d)^2} + f^2}{4\pi^2\left(f_r{}^2 - f^2\right)^2 + f^2\gamma^2} + \frac{2h\nu}{P} \tag{5}$$

where τ_d is the differential carrier lifetime, $(\Delta\nu)_{ST}$ is the modified Schawlow–Townes linewidth, ν is the optical frequency, h is the Planck constant and $\frac{2h\nu}{P}$ is the standard quantum noise limit at a laser output power of P.

Figure 4(a) shows the evaluated RIN of the same device characterized in the previous sections (device 3 in Table 1) for current injection levels above the threshold, ranging from 7.5 mA to 9 mA in 0.25 mA increments. The figure also includes curve fits based on Eq. (5), which provide key laser parameters: f_r, γ, $(\Delta\nu)_{ST}$ and $\chi\tau_d$ at various injection levels. Figure 4(b) plots the resonance frequencies f_r against $(I - I_{th})^{1/2}$, yielding a D-factor of 1.056 GHz/mA$^{1/2}$. Figure 4(c) illustrates the damping factor versus f_r^2, resulting in a K-factor of 0.648 ns. Figure 4(d) presents the extracted modified Schawlow-Townes linewidths, while Fig. 4(e) shows the differential carrier lifetimes at various bias levels above the threshold, assuming a transport factor of $\chi \approx 2$, derived from reflection coefficient (S11) measurements, which will be discussed in the next section. Finally, Fig. 4(f) shows a comparison of the D and K factors evaluated from S21 and RIN measurements for the devices listed in Table 1. The plot demonstrates a strong agreement and consistency in the extracted D and K values, with the exception of a few K values that deviate. This observation is supported by a root mean square error (RMSE) of 0.036 for the D values and 0.132 for the K values. The few deviations in the K values are likely due to inaccuracies in the curve fitting process.

Using Eqs. (2) and (3), the differential gain and the gain compression factors for the devices listed in Table 1 can be determined. This evaluation requires reasonably accurate estimates of key

Optics EXPRESS

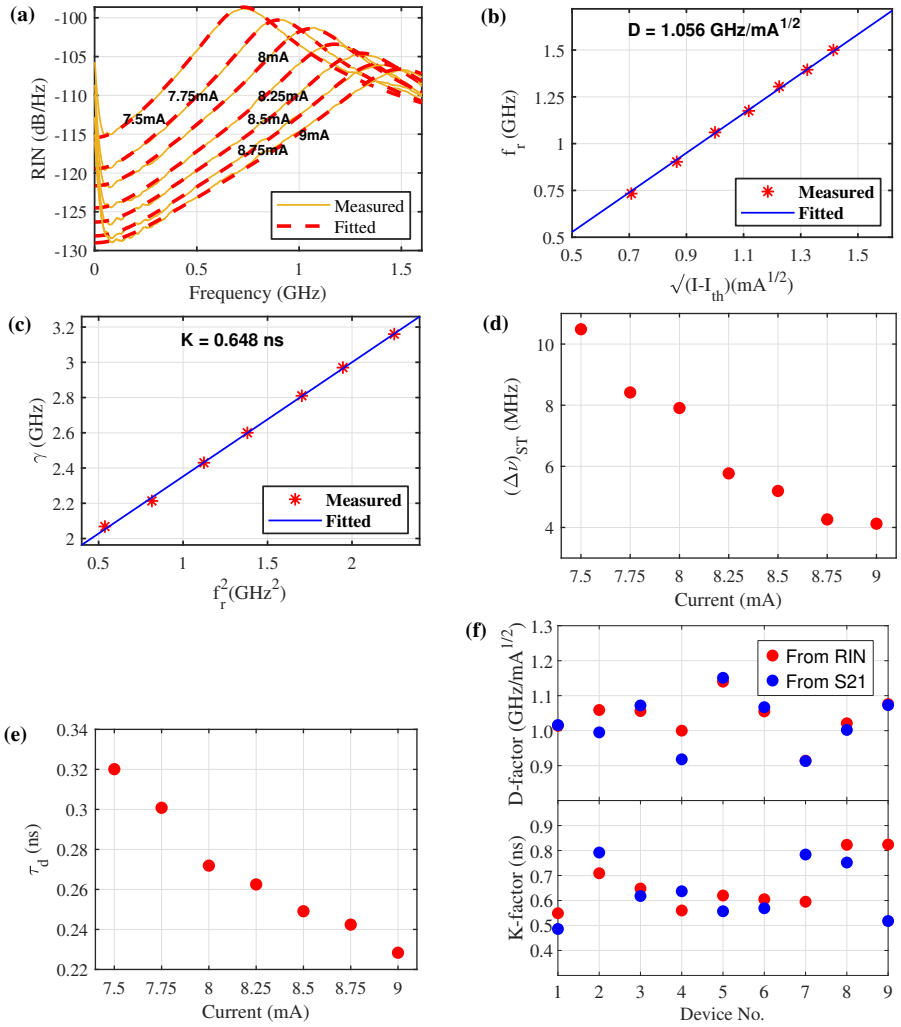

Fig. 4. (a) RIN curves at bias currents above threshold, with corresponding curve fits. (b) Extracted resonance frequencies as a function of the square root of the bias current minus the threshold current. (c) Extracted damping factors versus f_r^2. (d) Modified Schawlow Townes linewidths at bias points above the threshold. (e) Extracted differential carrier lifetimes at different bias levels above the threshold. (f) Comparison of D and K factors extracted from S21 and RIN measurements for devices listed in Table 1.

parameters, including the injection efficiency, the active region volume, the optical confinement factor, the group velocity and the photon lifetime.

The injection efficiencies for different contact pitch devices were evaluated using the technology computer-aided design (TCAD) Poisson solver in Synopsys Sentaurus software [22], with the results presented in Fig. 5(a). The QW active region volumes were determined by analyzing transmission electron microscopy (TEM) images of transverse cross-sections of nano-ridge lasers with 80 nm and 100 nm trench widths. These dimensions were also used to calculate the optical confinement factors and group velocities for the fundamental quasi-TE (transverse electric) mode of the waveguide cross-sections, employing the Lumerical MODE solver [23]. The optical confinement factors are depicted in Fig. 5(b). Finally, the differential gain values were calculated using Eq. (2) and are presented in Fig. 5(c). These values are in the range of 4.3 to 7×10^{-16} cm^2.

Optics EXPRESS

In the calculation of the differential gain, we have again considered a transport factor of $\chi \approx 2$ which is found from the reflection coefficient (S11) measurements discussed in the next section.

The gain compression factors can also be determined using Eq. (3), provided the photon lifetimes are known. Calculating the photon lifetime involves accounting for total cavity losses, which originate from various sources, including metal contact absorption losses, mirror losses, scattering and leakage to the substrate losses, and free-carrier absorption losses in the doped regions.

The absorption loss in the metal contacts depends on the mode-beating pair involved in the laser operation, as discussed in Section 2, and is subject to fabrication variations. To accommodate these variations, an error margin is introduced, with metal contact absorption losses estimated in the range of 10 - 20 cm^{-1} [16,17]. The laser cavity is formed by two facets: one is a cleaved facet, while the other is created by dry etching with an angle of 12° as mentioned in Section 2.

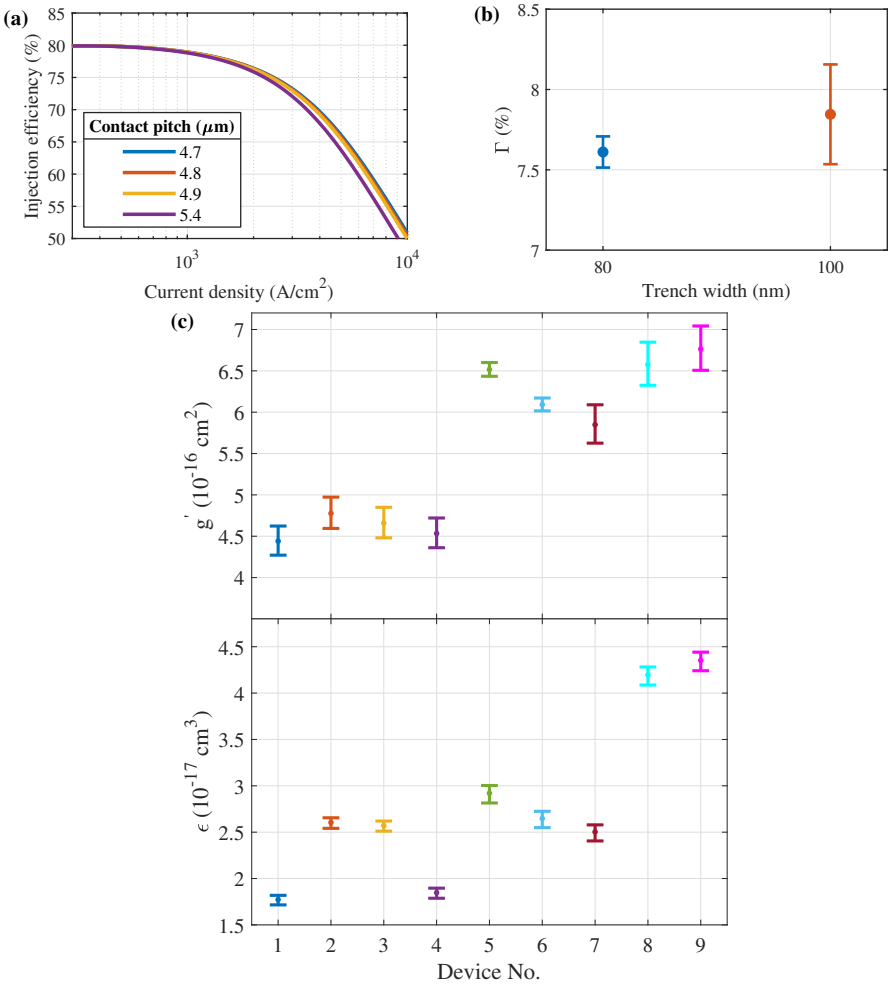

Fig. 5. (a) Injection efficiency vs. current density for different contact pitch devices evaluated using the TCAD Poisson solver. (b) Confinement factors for 80 nm and 100 nm trench width nano-ridges evaluated by Lumerical FDE MODE from TEM cross-sections of samples. (c) Evaluated differential gain and gain compression factor values for the devices listed in Table 1 at threshold.

Optics EXPRESS

Mirror losses are evaluated using the reflectivities of the cleaved and etched facets, calculated through Lumerical FDTD simulations based on dimensions obtained from TEM cross-sections.

Scattering and substrate leakage losses were derived from loss measurements of undoped nano-ridge waveguides, as reported in [17]. Free-carrier absorption losses in doped regions were computed using the FDE MODE solver by incorporating the imaginary components of the refractive indices of the doped materials, also detailed in [17]. Table 1 summarizes the evaluated losses, including losses from doped regions (α_d), scattering and substrate leakage losses (α_s), and mirror losses (α_m).

Using these total cavity losses, the photon lifetimes are calculated while accounting for the error margin associated with metal contact absorption losses. Based on these photon lifetimes, the gain compression factors are determined using Eq. (3) and are presented in Fig. 5(c). It can be seen that the gain compression factors lie between 1.8 and 4.4×10^{-17} cm^3 and tend to be higher for the longer cavity devices in Table 1 (devices 5 to 9). One of the factors contributing to gain saturation is spatial hole burning, induced by a standing wave pattern that creates a refractive index grating along the cavity [24]. The increase in the gain compression for the longer devices (devices 5 to 9) may be attributed to enhanced spatial hole burning, as longer cavities support more standing wave nodes and antinodes. Notably, previous studies have also reported a rise in the gain compression factor with increasing cavity length for $In_{0.2}Ga_{0.8}As/GaAs$ quantum well lasers [25].

5. Extraction of recombination coefficients

For the extraction of the recombination coefficients of the nano-ridge lasers, a fully calibrated subthreshold reflection coefficient (S11) measurement was performed using a network analyzer to evaluate the input impedance. Taking the extracted effective carrier capture time from the modulation response, the differential carrier lifetime and the carrier escape time for quantum well lasers can be extracted from the real part of the input impedance by using [20]:

$$Z(\omega) = R_s + \frac{R_d\left(1 + j\omega\frac{\tau_d\tau_e}{\tau_d+\tau_e}\right)}{(1+j\omega\tau_d)(1+j\omega\tau_s) + j\omega\frac{\tau_s\tau_d}{\tau_e}} \tag{6}$$

where Z is the input impedance, R_s is frequency and bias independent series resistance and R_d is frequency and bias dependent resistance associated with the differential laser impedance. The other parameters are defined in the previous sections. R_s is extracted to be 5.1 Ω from an S11 measurement performed on the device discussed in the previous sections (device 3 in Table 1) up to 10 GHz, as shown in Fig. 6(a). By taking the extracted effective carrier capture of 115 ps from the small signal modulation response measurements in Section 3, S11 measurements were then performed for the same device, allowing the extraction of R_d, τ_d and τ_e at subthreshold current levels up to 3.5 mA. Figure 6(b) illustrates the extraction of these parameters at a bias current of 2 mA.

After determining the differential carrier lifetimes at various bias points, the carrier density can be calculated by [26]:

$$N(I) = \frac{\eta_i \int_0^I \tau_d(I)\, dI}{qV} \tag{7}$$

where N is the carrier density and I is the bias current.

With a subthreshold injection efficiency of 80%, obtained from electrical simulations (Fig. 5(a)), and the active region volume determined from TEM cross-sections of the samples, the carrier density was calculated for each bias current, as shown in Fig. 6(c). The recombination coefficients were subsequently extracted by analyzing the differential carrier lifetime as a function of the

Optics EXPRESS

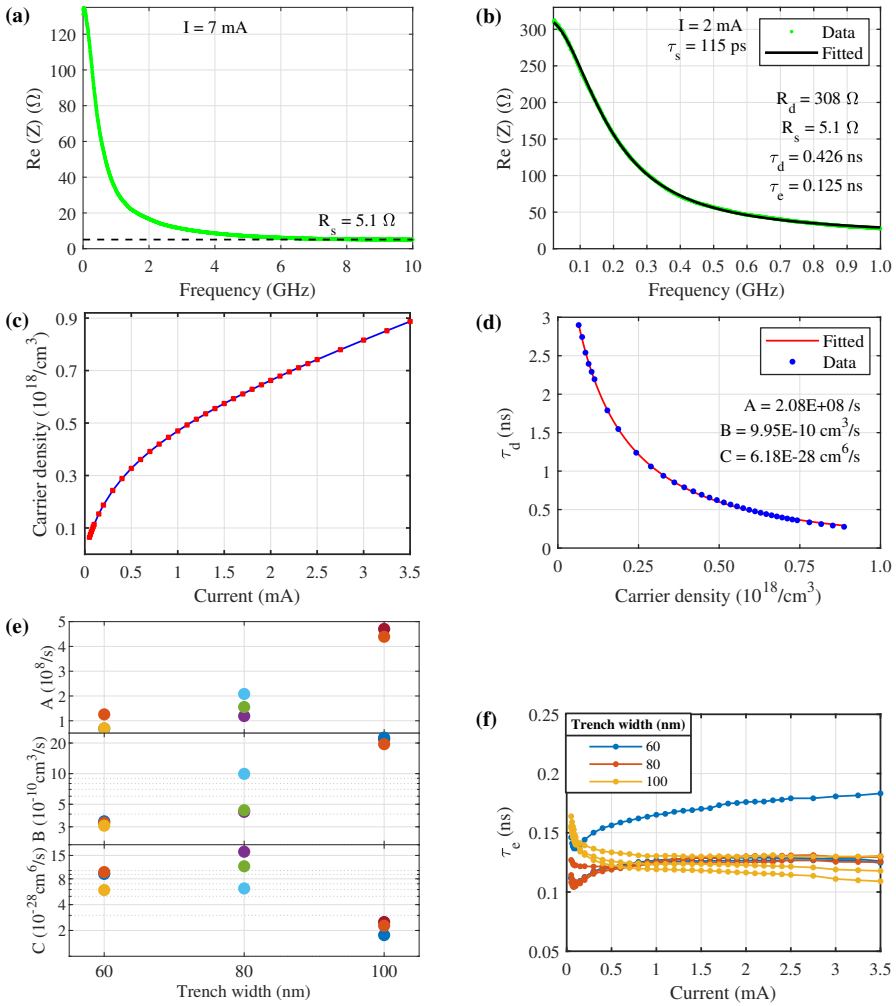

Fig. 6. (a) Extraction of R_s from an S11 measurement up to 10 GHz (b) Extraction of R_d, τ_e and τ_d at $I = 2$ mA (c) Calculated carrier density at each bias point. (d) Extraction of A, B and C coefficients (e) Extracted A,B and C coefficients versus the trench width. (f) Extracted carrier escape times versus the bias points for the different trench width nano-ridge lasers.

carrier density, using the standard recombination formula [26].

$$\tau_d(N) = \frac{1}{A + 2BN + 3CN^2} \tag{8}$$

where A, B and C are recombination coefficients associated with defects, radiative recombination and Auger recombination respectively. Figure 6(d) illustrates the extraction of the recombination coefficients by employing Eq. (8). A summary of all extracted parameters for this device is presented in Table 2.

To assess the impact of the trench width on the recombination coefficients, three groups of devices with trench widths of 60 nm, 80 nm, and 100 nm were characterized, each comprising three devices. To minimize fabrication-related variations, the electrical characterizations were performed on adjacent devices within the same die on which device 3 in Table 1 is located.

Optics EXPRESS

Table 2. List of extracted parameters for device 3 in Table 1

τ_s (ps)	τ_e (ps)	g' (10^{-16} cm^2)	ε (10^{-17} cm^3)	A (10^8 /s)	B (10^{-10} cm$^3/s$)	C (10^{-28} cm^6/s)
115	125	4.66	2.57	2.08	9.95	6.18

Among the nine characterized devices, one with 80 nm trench width and all those with 100 nm wide trenches function as lasers, while the rest operate as light-emitting diodes.

Figure 6(e) illustrates the dependence of the A, B, and C coefficients on the trench width. Notably, the A coefficient appears to increase with trench width, possibly due to the presence of confined threading dislocation defects being trapped closer to the trench opening (or the nano-ridge volume) as the trenches widen or worse InGaP surface passivation at the lower {111} facets. Additionally, nano-ridges with 100 nm trenches exhibit lower C and higher B values. This may be attributed to device heating from hot spots near the sparse metal plugs, which likely decreases as the device volume increases.

For the $In_{0.2}Ga_{0.8}As$/GaAs material system, the A coefficient is generally expected to be negligible while reported values for B and C vary [18,27]. When we compare the extracted coefficients with the reported values in [27], the B values for the 60 nm and 80 nm trenches are generally in good agreement except for one device, which is about twice as high, but for the 100 nm trenches, our values are up to four times larger. On the other hand, our extracted C coefficients are typically one to two orders of magnitude higher. It is worth noting that these references use the standard approach of extracting recombination coefficients based on a single-carrier-level rate equation model originally developed for bulk active region lasers. However, as shown in [28], this bulk analysis may not be valid for quantum well lasers due to the influence of carrier populations in the barrier and separate confinement heterostructure (SCH) regions. By accounting for carrier transport effects, [28] demonstrates that the corrected recombination coefficients can differ significantly—yielding B values approximately twice as high, and C values around 100 times larger than those obtained using the bulk model. This may offer a reasonable explanation for the higher B and C values we have observed in our nano-ridge lasers. In evaluating the recombination coefficients, it is also important to note that the thickness of the three quantum wells was used as the effective active region thickness.

At a threshold carrier density of approximately 2×10^{18} cm^{-3}, defect-related recombination accounts for less than 5% of the total threshold current in the nano-ridge lasers with trench widths of 60 nm and 80 nm, and remains below 10% for 100 nm trench widths. This result underscores the effectiveness of aspect ratio trapping and nano-ridge engineering in mitigating defect-related losses. Consequently, these techniques enable the integration of high-quality III-V nano-ridge structures on silicon substrates, offering a promising pathway for advancing monolithic III-V on silicon photonic devices.

The extracted carrier escape times are shown in Fig. 6(f). With the exception of one outlier, the measured values range from 110 – 130 ps, yielding a τ_s/τ_e ratio close to unity. This aligns with the findings reported in [29] for $In_{0.25}Ga_{0.75}As$/GaAs quantum well lasers and directly impacts the differential gain discussed in the previous section. A τ_s/τ_e ratio near unity reduces the differential gain by a factor of two compared to the bulk counterparts, which may explain the lower D-factor and the higher K-factor values observed in Fig. 4(f). In [19], it was shown that for $In_{0.2}Ga_{0.8}As$/GaAs quantum well lasers, the K-factor increased from 0.24 ns to 0.6 ns simply by increasing the carrier transport time through a wider SCH layer. Increasing the resonance frequency and reducing the K-factor to enhance the modulation bandwidth and improve the damping-limited maximum bandwidth require shorter effective carrier capture times. Therefore, transitioning to a continuous contact scheme with smaller τ_s values could enable faster laser performance.

Optics EXPRESS

6. Conclusion

In this study, the static and dynamic characteristics of monolithic nano-ridge lasers were analyzed, revealing several critical insights into their behavior.

Effective carrier capture times extracted from S21 measurements were predominantly between 100 to 125 ps, exceeding typical quantum well laser values. This increase is attributed to the sparse placement of metal plugs in the contacting scheme, which leads to longer carrier transport times. This underscores the critical impact of contacting configurations on carrier transport dynamics and overall device performance.

Relative intensity noise (RIN) measurements yielded D-factors of approximately 1 GHz/mA$^{1/2}$ and K-factors ranging from 0.5 to 0.8 ns, consistent with values derived from S21 measurements. Using these results, differential gain values in the range of 4.3 to 7×10^{-16} cm^2 and gain compression factor values in the range of 1.8 to 4.4×10^{-17} cm^3 were evaluated.

Finally, recombination coefficients were extracted for nano-ridge lasers with trench widths of 60 nm, 80 nm and 100 nm, revealing the effect of device geometry on the device behavior. Wider (100 nm) trench nano-ridges showed higher A coefficients, likely due to trapped threading dislocations near the trench opening (or the nano-ridge volume) or degrading surface passivation. Additionally, devices with wider trenches (100 nm) exhibited lower C coefficients and higher B coefficients, potentially due to reduced heating effects as the device volume increased. More importantly, it was demonstrated that defect-related recombination accounted for less than 5% of the total threshold current in nano-ridge lasers with trench widths of 60 nm and 80 nm, and less than 10% for those with 100 nm trenches. These findings emphasize the effectiveness of aspect ratio trapping and nano-ridge engineering in suppressing defects, enabling the integration of high-quality III-V nano-ridge structures on silicon substrates and advancing the development of monolithic III-V on silicon photonic devices.

Compared to the values reported in [27], our extracted B coefficients for the 60 nm and 80 nm trenches are largely consistent , while those for the 100 nm trenches are up to four times higher. Our C coefficients are typically one to two orders of magnitude larger. This discrepancy may stem from the limitations of bulk-based models used in prior studies, which, as shown in [28], underestimate extracted recombination coefficients in quantum well structures by neglecting the influence of carrier populations in the barrier and SCH regions.

The extracted carrier escape times are mostly within the range of 110 – 130 ps, yielding a τ_s/τ_e ratio close to unity. This has reduced the differential gain by a factor of two compared to the bulk counterparts, lowering the modulation bandwidth and increasing the K-factor. Thus, adopting a continuous contact scheme with smaller τ_s values could enhance the laser performance.

Funding. H2020 Excellent Science (884963).

Acknowledgments. This work was supported by the EU H2020 program under grant agreement No. 884963 (ERC AdG NARIOS). G. Morthier acknowledges Interreg-Lightup and PhotonDelta for financial support.

Disclosures. The authors declare no conflicts of interest.

Data availability. Data underlying the results presented in this paper are not publicly available at this time but may be obtained from the authors upon reasonable request.

References

1. S. Y. Siew, B. Li, F. Gao, *et al.*, "Review of silicon photonics technology and platform development," J. Lightwave Technol. **39**(13), 4374–4389 (2021).
2. S. Lin, X. Zheng, J. Yao, *et al.*, "Efficient, tunable flip-chip-integrated III-V/Si hybrid external-cavity laser array," Opt. Express **24**(19), 21454–21462 (2016).
3. S. Bao, Y. Wang, K. Lina, *et al.*, "A review of silicon-based wafer bonding processes, an approach to realize the monolithic integration of Si-CMOS and III–V-on-Si wafers," J. Semicond. **42**(2), 023106 (2021).
4. C. Xiang, W. Jin, D. Huang, *et al.*, "High-performance silicon photonics using heterogeneous integration," IEEE J. Sel. Top. Quantum Electron. **28**(3), 1–15 (2022).
5. D. Liang and J. E. Bowers, "Recent progress in heterogeneous III-V-on-silicon photonic integration," Light: Adv. Manufact. **2**(1), 59 (2021).

Optics EXPRESS

6. G. Roelkens, J. Zhang, L. Bogaert, *et al.*, "Micro-transfer printing for heterogeneous Si photonic integrated circuits," IEEE J. Sel. Top. Quantum Electron. **29**(3: Photon. Elec. Co-Inte. and Ad), 1–14 (2023).
7. J. Zhang, G. Muliuk, J. Juvert, *et al.*, "III-V-on-Si photonic integrated circuits realized using micro-transfer-printing," APL Photonics **4**(11), 110803 (2019).
8. J. Van der Ziel, R. Dupuis, R. Logan, *et al.*, "Degradation of GaAs lasers grown by metalorganic chemical vapor deposition on Si substrates," Appl. Phys. Lett. **51**(2), 89–91 (1987).
9. C. Shang, J. Selvidge, E. Hughes, *et al.*, "A pathway to thin GaAs virtual substrate on on-axis Si (001) with ultralow threading dislocation density," Physica Status Solidi (a) **218**(3), 2000402 (2021).
10. W.-Q. Wei, A. He, B. Yang, *et al.*, "Monolithic integration of embedded III-V lasers on SOI," Light: Sci. Appl. **12**(1), 84 (2023).
11. P. Wen, P. Tiwari, S. Mauthe, *et al.*, "Waveguide coupled III-V photodiodes monolithically integrated on Si," Nat. Commun. **13**(1), 909 (2022).
12. Y. Xue, Y. Han, Y. Wang, *et al.*, "High-speed and low dark current silicon-waveguide-coupled III-V photodetectors selectively grown on SOI," Optica **9**(11), 1219–1226 (2022).
13. B. Kunert, W. Guo, Y. Mols, *et al.*, "Integration of III/V hetero-structures by selective area growth on Si for nano-and optoelectronics," ECS Trans. **75**(8), 409–419 (2016).
14. Y. Shi, Z. Wang, J. Van Campenhout, *et al.*, "Optical pumped InGaAs/GaAs nano-ridge laser epitaxially grown on a standard 300-mm Si wafer," Optica **4**(12), 1468–1473 (2017).
15. D. Colucci, M. Baryshnikova, Y. Shi, *et al.*, "Unique design approach to realize an O-band laser monolithically integrated on 300 mm Si substrate by nano-ridge engineering," Opt. Express **30**(8), 13510–13521 (2022).
16. Y. De Koninck, C. Caer, D. Yudistira, *et al.*, "GaAs nano-ridge laser diodes fully fabricated in a 300-mm CMOS pilot line," Nature **637**(8044), 63–69 (2025).
17. A. A. Yimam, D. Colucci, C. Caer, *et al.*, "Semi-analytical model for electrically injected GaAs nano-ridge laser diodes monolithically integrated on silicon," Opt. Express **33**(2), 2101–2114 (2025).
18. L. A. Coldren, S. W. Corzine, and M. L. Mashanovitch, "Diode lasers and photonic integrated circuits," (John Wiley & Sons, 2012), chap. 5.
19. R. Nagarajan, M. Ishikawa, T. Fukushima, *et al.*, "High speed quantum-well lasers and carrier transport effects," IEEE J. Quantum Electron. **28**(10), 1990–2008 (1992).
20. I. Esquivias, S. Weisser, B. Romero, *et al.*, "Carrier dynamics and microwave characteristics of GaAs-based quantum-well lasers," IEEE J. Quantum Electron. **35**(4), 635–646 (1999).
21. F.-L. Wang, X.-W. Ma, Y.-Z. Huang, *et al.*, "Relative intensity noise in high-speed hybrid square-rectangular lasers," Photonics Res. **6**(3), 193–197 (2018).
22. "Synopsys tcad," https://www.synopsys.com/manufacturing/tcad.html. Accessed: 2023-6-4.
23. "Lumerical photonics simulation and design software official website," https://www.ansys.com/products/photonics. Accessed: 2025-1-20.
24. H. Sun, "Gain saturation enhancement of longitudinal hole burning via standing wave induced wave coupling in a semiconductor laser," IEEE J. Quantum Electron. **32**(4), 617–619 (1996).
25. E. Kapon, eds., "Semiconductor Lasers I Fundamentals," (Academic Press, 1999), chap. 3, pp. 177–290.
26. G. Shtengel, D. Ackerman, P. Morton, *et al.*, "Impedance-corrected carrier lifetime measurements in semiconductor lasers," Appl. Phys. Lett. **67**(11), 1506–1508 (1995).
27. D. Ding, S. R. Johnson, J.-B. Wang, *et al.*, "Determination of spontaneous emission quantum efficiency in InGaAs/GaAs quantum well structures," in *Solid State Lighting and Solar Energy Technologies*, vol. 6841 (SPIE, 2008), pp. 83–90.
28. J. Pikal, C. Menoni, H. Temkin, *et al.*, "Carrier lifetime and recombination in long-wavelength quantum-well lasers," IEEE J. Sel. Top. Quantum Electron. **5**(3), 613–619 (1999).
29. B. Romero, I. Esquivias, S. Weisser, *et al.*, "Carrier capture and escape processes in $In_{0.25}Ga_{0.75}As$/GaAs quantum-well lasers," IEEE Photonics Technol. Lett. **11**(7), 779–781 (1999).